

Ferromagnetic Resonance in a Magnetically Dilute Percolating Ferromagnet: An Experimental and Theoretical Study

Y.K. Edathumkandy¹, K. Das¹, K. Gas^{1,2}, D. Sztenkiel¹,
D. Hommel^{3,4}, H. Przybylińska¹ and M. Sawicki^{1,5}

¹*Institute of Physics, Polish Academy of Sciences,
Aleja Lotników 32/46, PL-02668 Warsaw, Poland*

²*Center for Science and Innovation in Spintronics, Tohoku University, Sendai 980-8577, Japan*

³*Łukasiewicz Research Network - PORT Polish Center for Technology Development, Stalówicka 147, Wrocław 54-066, Poland*

⁴*Institute of Low Temperature and Structure Research,
Polish Academy of Sciences, Okólna 2, Wrocław 50-422, Poland*

⁵*Research Institute of Electrical Communication, Tohoku University,
Katahira 2-1-1, Aoba-ku, Sendai 980-8577, Japan*

Ferromagnetic resonance (FMR) serves as a powerful probe of magnetization dynamics and anisotropy in percolating ferromagnets, where short-range interactions govern long-range magnetic order. We apply this approach to $\text{Ga}_{1-x}\text{Mn}_x\text{N}$ ($x \simeq 8\%$), a dilute ferromagnetic semiconductor, combining FMR and superconducting quantum interference device magnetometry. Our results confirm the percolative nature of ferromagnetism in $(\text{Ga},\text{Mn})\text{N}$, with a Curie temperature $T_C = 12$ K, and reveal that despite magnetic dilution, key features of conventional ferromagnets are retained. FMR measurements establish a robust uniaxial anisotropy, dictated by Mn^{3+} single-ion anisotropy, with an easy-plane character at low Mn content. While excessive line broadening suppresses FMR signals below 9 K, they persist up to 70 K, indicating the presence of non-percolating ferromagnetic clusters well above T_C . The temperature dependence of the FMR intensity follows that of the magnetization, underscoring the stability of these clusters. We quantitatively describe both FMR and SQUID observables using atomistic spin model operating on a common set of parameters. The level of agreement, achieved without tuning parameters between datasets, demonstrates the robustness and practical applicability of the approach in capturing the essential physics of spin-diluted, percolating ferromagnets. This study advances the understanding of percolating ferromagnetic systems, demonstrating that FMR is a key technique for probing their unique dynamic and anisotropic properties. Our findings contribute to the broader exploration of dilute ferromagnets and provide new insights into percolating ferromagnetic systems, which will be relevant for spintronic opportunities.

I. INTRODUCTION

Achieving direct spin control in optoelectronic devices would mark a significant technological breakthrough. In this context dilute ferromagnetic semiconductors (DFS) have attracted substantial research interest because they combine the functionalities of semiconductors (or insulators) with spin degrees of freedom [1, 2], thus paving the way to technological applications [3]. Within the systems being considered [4], $(\text{Ga},\text{Mn})\text{N}$ or $\text{Ga}_{1-x}\text{Mn}_x\text{N}$, with x representing the fraction of manganese ions distributed randomly on gallium sites, has gained substantial interest. This is mainly due to the high thermal stability of the wide band gap GaN host, that makes it suitable for use in extreme environments, such as outer space or harsh industrial settings.

Despite numerous attempts [5], achieving room-temperature ferromagnetism (FM) in DFS remains an elusive goal in materials science. In the case of Mn-doped

GaN, this is primarily due to the insulating character of both GaN:Mn [6] and $(\text{Ga},\text{Mn})\text{N}$ mixed crystals [7–9], which precludes magnetic coupling via itinerant carriers. In the wurtzite GaN lattice Mn is tetrahedrally coordinated by 4 neighboring nitrogen ions. In the absence of other intentional doping or charged point defects, Mn assumes a neutral acceptor oxidation state, Mn^{3+} (d^4 configuration) [10, 11], whose dominant coupling mechanism is short-range superexchange [7, 12, 13]. This coupling has been confirmed to be *ferromagnetic* for at least 25 coordination shells [14].

These unique physical conditions allow the formation of a network in which FM interactions can propagate in a percolation-like manner across the real samples at nonzero temperatures [13, 15–18], even for Mn concentrations well below 18%, the percolation threshold for the nearest-neighbor-only scenario. We owe it to the fact that although the exchange integral decreases strongly with distance (r) across further coordination shells, at the

same time the number of possible Mn ions in those shells increases. Overall, the effective coupling in (Ga,Mn)N decays slower with distance, approximately as $\exp(-r/b)$, with b as high as 1.1 Å [19]. This situation is very different from the canonical dilute ferromagnetic semiconductor (Ga,Mn)As [20, 21], where a robust global FM state can be stabilized above 170 K [22] by hole-mediated, long-range coupling operating over the same range of Mn compositions [2].

There are a few profound implications of the percolating form of FM in (Ga,Mn)N to our study. Whereas all of the spins are expected to be coupled at $T = 0$, only a fraction of the spins present in the material supports the FM state at nonzero temperatures. Starting from high temperatures, Mn spins form clusters of various shape and sizes and the Curie temperature T_C , marks that temperature at which the first infinite, percolating ("wall-to-wall") FM cluster forms. Therefore, at nonzero temperatures such a magnetic system is expected to behave as an ensemble of infinite and finite FM clusters (macrospins), characterized by a wide range of blocking temperatures and relaxation times.

This makes the magnetism, in general, and T_C , in particular, to depend on the characteristic measurement time (t_m) of the experimental technique in use. Similar to the blocking behavior in magnetically granular systems, the longer the t_m , the lower the characteristic temperature (in this case T_C), as more macrospins are given sufficient amount of time to reach equilibrium, in which they average out their contributions to the measured magnetic properties (e.g. magnetic moment m in case of magnetometry). Consequently, the magnetism—and the determination of T_C —depends on t_m due to macrospin-relaxation processes. Interestingly, this phenomenon was also observed in (Ga,Mn)As, where, due to various technological factors [23, 24] or deliberate measurement design [25–27], the material can be pushed toward the localization limit of holes. At this boundary, magnetic coupling is maintained only on mesoscopic scales [25, 28–30].

Another important factor is that Mn ions in GaN retain their single-ion magnetic anisotropy (SIMA), which is only weakly modified by their mutual FM coupling. Mn^{3+} ions in GaN adopt a high-spin configuration ($S = 2$, $L = 2$), with the 5T_2 state being the ground state. In the paramagnetic regime, a strong uniaxial magnetic anisotropy (UMA) emerges at low temperatures, differentiating the magnetic response depending on whether the external magnetic field \mathbf{H} is applied parallel or perpendicular to the hexagonal c -axis of the GaN crystal, i.e., $\mathbf{H} \parallel \mathbf{c}$ or $\mathbf{H} \perp \mathbf{c}$, respectively. This anisotropy arises from the trigonal distortion inherent to the wurtzite GaN

lattice structure.

In the ideal tetrahedral coordination the ratio of the hexagonal lattice parameters $c/a = \sqrt{8/3}$. In pure GaN and at low Mn concentrations, $c/a < \sqrt{8/3}$, resulting in UMA with an easy-plane character, favoring spin alignment within the basal plane and making the c -axis the hard axis. However, upon increasing Mn concentration, the situation changes significantly. For Mn content, x_{Mn} , exceeding about 10%, a transition to an elongated tetrahedron is anticipated in (Ga,Mn)N [16], which leads to a tensile trigonal distortion capable of reversing the easy magnetization direction to the c -axis.

Between these two regimes, an intriguing scenario may arise where the trigonal distortion is marginal, effectively nullifying UMA. Under such conditions, a significantly weaker threefold magnetic anisotropy could be potentially observed, originating from the static Jahn-Teller (JT) effect. This effect displaces N ions surrounding the Mn ion, thereby lowering its site symmetry from trigonal to rhombic [31, 32]. Although the JT-related anisotropy is relatively weak in the ground state, it plays a pivotal role in magnetization switching processes in FM (Ga,Mn)N [33].

Prior studies have definitively shown the importance of investigating static micro-magnetic properties in (Ga,Mn)N layers [7, 13, 17, 34]. The manipulation of magnetic anisotropy in (Ga,Mn)N using electric fields was successfully demonstrated in both the paramagnetic [35] and FM case [33]. Furthermore, using the spin Hall magnetoresistance technique [36], the spectrum of (Ga,Mn)N functionalities was recently supplemented by the demonstration of efficient generation and detection of spin currents in Pt/(Ga,Mn)N structures up to 50 K [37], i.e., well above the Curie temperature established upon magnetometry method. Despite these advancements, our understanding of the dynamics and relaxation processes of magnetization within (Ga,Mn)N, along with the intricate physics governing magnetic anisotropy, remains in its infancy. To address these shortcomings, the ferromagnetic resonance (FMR) technique is employed, a highly precise method renowned for its capability [widely used for its ability] to probe the dynamic magnetic properties of ferromagnetic thin films [38].

FMR is the ideal method for comprehensively assessing fundamental characteristics, including absolute values of magnetic anisotropies, Curie temperature, magnetoelastic coupling coefficients, and parameters describing magnetization relaxation [39]. While FMR techniques have been instrumental in exploring the dynamics and relaxation processes of magnetization in other DFS [39–42], the realm of (Ga,Mn)N remains largely uninvestigated in

this context. This is primarily due to the fact that, unlike Mn^{2+} (d^5 configuration), the paramagnetic Mn^{3+} ion in GaN tetrahedral coordination is EPR silent in typical X-band spectrometers. Consequently much of the information available today on the properties of the Mn^{3+} state in GaN was established by optical spectroscopy [43, 44] and low-temperature and high-field magnetometry [31, 34, 43, 45]. In this context, the robust FM state observed in (Ga,Mn)N [17] allows us to address the material using classical EPR equipment by studying FMR, the collective response of the otherwise EPR-silent Mn^{3+} ions. Our study, therefore, aims to expand the pool of understanding of this dilute magnetic percolating system well beyond the limits of static SQUID measurements (t_m of the order of seconds) into the realm of GHz, specific to FMR technique.

There exists a range of well-established and successfully tested theoretical approaches that describe individual aspects of (Ga,Mn)N magnetism. The crystal-field model (CFM), originally developed for Cr^{2+} in II-VI semiconductors [46–48] and later adapted to Mn^{3+} in GaN [31, 33–35, 43, 44, 49, 50], provides precise predictions of $m(H)$ in high-field conditions but treats Mn ions essentially as non-interacting. Extending this approach to include interactions involves constructing a Hamiltonian matrix whose dimension grows exponentially with the number of Mn spins included, i.e., $25^n \times 25^n$, where n is the number of nearest-neighbor spins considered in the system. This renders the computation intractable beyond $n \approx 4$, and omits interactions with more distant neighbors entirely [7, 33, 50, 51]. While this method can achieve good agreement with experimental data for fields above about 30 kOe [50], it fails to capture magnetization at low fields. Notably, CFM predicts vanishing remnant magnetization, $M_{\text{REM}} = 0$, at any temperature, in contradiction with experimental data showing $M_{\text{REM}} \simeq 20\%$ of $M(H \simeq 50 \text{ kOe})$ at $T = 2 \text{ K}$ [17, 18] which gradually decreases with temperature and disappears at T_C . To account for ferromagnetic ordering and the Curie temperature in (Ga,Mn)N, an alternative approach based on Monte Carlo simulations was adopted. This method employs tight-binding-derived exchange integrals combined with Metropolis spin updates and has been shown to reproduce the experimental T_C values accurately across the experimentally accessible range $0.01 \leq x \leq 0.10$ [17, 52], outperforming mean-field approaches based on *ab initio* inputs, which tend to overestimate T_C by up to an order of magnitude [53]. Nevertheless, neither of these approaches alone is capable of simultaneously describing the full range of magnetic properties—such as magnetization curves, remnant magnetization, coercive fields, Curie temperatures, and, crucially for this

study, collective spin dynamics (i.e., FMR resonance fields and linewidths)—within a single, unified set of parameters. To address this issue, we employ an atomistic spin model [54] based on classical spin vectors, combined with the stochastic Landau–Lifshitz–Gilbert (sLLG) formalism [33, 51], which allows us to capture both equilibrium magnetic properties and precessional dynamics. This framework enables us to explore to what extent a unified model can account for both static magnetization and FMR behavior in the magnetically dilute, percolating ferromagnet (Ga,Mn)N.

In this work, the FMR technique and superconducting quantum interference device (SQUID) magnetometry are employed as complementary methods to probe magnetic properties of the insulating ferromagnetic $\text{Ga}_{1-x}\text{Mn}_x\text{N}$ layer with an Mn concentration of $x = 7.9\%$. Our primary focus lies in analyzing the temperature dependence of the resonance field and its correlation with the angular orientation of the applied magnetic field. This approach allows us to determine critical parameters such as the Curie temperature, the effective g -factor, and magnetic anisotropy constants across varying temperatures. Moreover, our investigation extends to explore the temperature- and angle-dependent linewidth of the FMR signal. This analysis is crucial for revealing insights into material inhomogeneities and relaxation mechanisms in (Ga,Mn)N. Importantly, we also demonstrate that the broad sets of experimental observables—those obtained via SQUID magnetometry and FMR—can be consistently reproduced using a single atomistic spin model with one common set of parameters. Despite the rudimentary representation of the crystalline structure and Mn ion distribution and other simplifications, this unified approach provides remarkably good agreement with experimental data, underscoring the robustness and applicability of the model in describing of such challenging systems as spin-diluted percolating magnets.

II. METHODS

A. Experiment

1. Samples

(Ga,Mn)N layers with various thicknesses up to about $1 \mu\text{m}$ are grown by the molecular beam epitaxy (MBE) technique on fully relaxed GaN templates (about $2 \mu\text{m}$ thick) deposited by MOVPE on c -plane $0.3 - 0.4 \text{ mm}$ thick Al_2O_3 substrates, following the specifications elaborated previously to obtain single phase epitaxial layers without traceable amounts of other magnetic phases [16, 18]. The surface quality of the layers was monitored

in situ during growth using reflection high-energy electron diffraction. High quality and single phase of the material are confirmed by high-resolution X-ray diffraction.

2. Experimental procedures

Magnetic measurements are performed in a Quantum Design superconducting quantum interference device (SQUID) MPMS-XL magnetometer with a low field option to measure magnetic properties at magnetic fields up to 70 kOe and temperatures between 2 and 400 K. Strict protocols are followed to avoid artifacts and limitations of volume SQUID magnetometry of thin films deposited on bulky substrates [55–57]. Measurements of a bare GaN template substrate serve as a reference signal to eliminate the interference of disturbing low-temperature magnetic anisotropy of commercial sapphire substrates [58]. The remaining relevant details are given in Appendix A.

Ferromagnetic resonance experiments are conducted with use of a BRUKER EMX plus spectrometer operating at 9.5 GHz ($h\nu = 39 \mu\text{eV}$) and equipped with an Oxford Instruments 910 Cryostat enabling temperature control from 3 to 300 K and 360 deg sample rotation with respect to the static external magnetic field \mathbf{H} . The recorded FMR signal is the magnetic field derivative of the absorbed microwave power that is proportional to the imaginary part of the AC magnetic susceptibility χ'' .

B. Numerical simulations

The experimental data are modeled using an atomistic spin model [54] combined with the stochastic Landau-Lifshitz-Gilbert (sLLG) equation [33, 51]. Simulations are performed on a system consisting of 9860 randomly distributed Mn spins in a wurtzite lattice, with in-plane periodic boundary conditions to model a large thin film. The classical spin Hamiltonian accounts for Zeeman energy, magnetocrystalline anisotropy, and ferromagnetic superexchange interactions between Mn ions taken exactly up to the 14th coordination sphere [19]. The spin dynamics are governed by the sLLG equation, and the magnetization and FMR response are computed as a function of external magnetic field and temperature. A Monte Carlo method is employed to simulate thermoremanent magnetization. [59, 60].

Of particular importance in this study is an attempt to model FMR measurements. To this end the simulation box is numerically subjected to an AC magnetic field [61], and the resonance field and line-width are extracted from

the simulation results.

Details of the simulation methodology, including the full Hamiltonian, equations of motion, and parameter values, are provided in Appendix B, while additional discussion of the model assumptions and limitations is given in Appendix C.

III. RESULTS AND DISCUSSIONS

A. Magnetic characterization

The Curie temperature, T_C , is the main parameter describing any ferromagnetic material [62], yet its determination has remained a challenge despite numerous advances in this field. The challenge grows in magnetically dilute materials when the critical features become smeared over a wide temperature range. In this study, we employ the thermoremanent magnetization (TRM) measurements as the least cumbersome method of the determination of T_C in DFS, regardless of the range of the FM interaction [17, 18, 63, 64].

To acquire TRM data the sample is initially field-cooled in a magnetic field of $H_{FC} = 3 \text{ kOe}$ [blue squares in Fig. 1 (a)]. After quenching the field at $T = 2 \text{ K}$ the values of the remnant magnetisation M_{TRM} is recorded during warming [green bullets in Fig. 1 (a)]. The temperature at which M_{TRM} vanishes indicates $T_C = 12 \text{ K}$ in this film. More in-depth experimental considerations pertinent to this technique are outlined in Appendix A.

Exemplary magnetization curves, $M(H)$, obtained for the same sample at $T = 5 \text{ K} < T_C$ are shown in Fig. 1 (b) as solid symbols. Despite being in the FM state, (Ga,Mn)N exhibits a considerable rounded $M(H)$ at low magnetic fields [15–18, 33, 50, 65]. This behavior arises directly from the significant magnetic dilution and short-range character of the superexchange interaction, both giving rise to the percolative nature of the FM coupling.

On a microscopic level, this effect manifests itself as a broad distribution of ferromagnetically coupled clusters of varying sizes, meaning that at weak magnetic fields, hysteresis involves only a fraction of the spins. At this level of dilution, (Ga,Mn)N does not form a uniform ferromagnetic phase below T_C . Moreover, the $M(H)$ data indicate that magnetization does not fully saturate even at fields as high as 70 kOe. This behavior arises from the significant contribution of the weakly saturating orbital moment to the total magnetic moment of Mn^{3+} ions [66].

The results of the atomistic spin simulations corresponding to the relevant magnetization data—namely, the

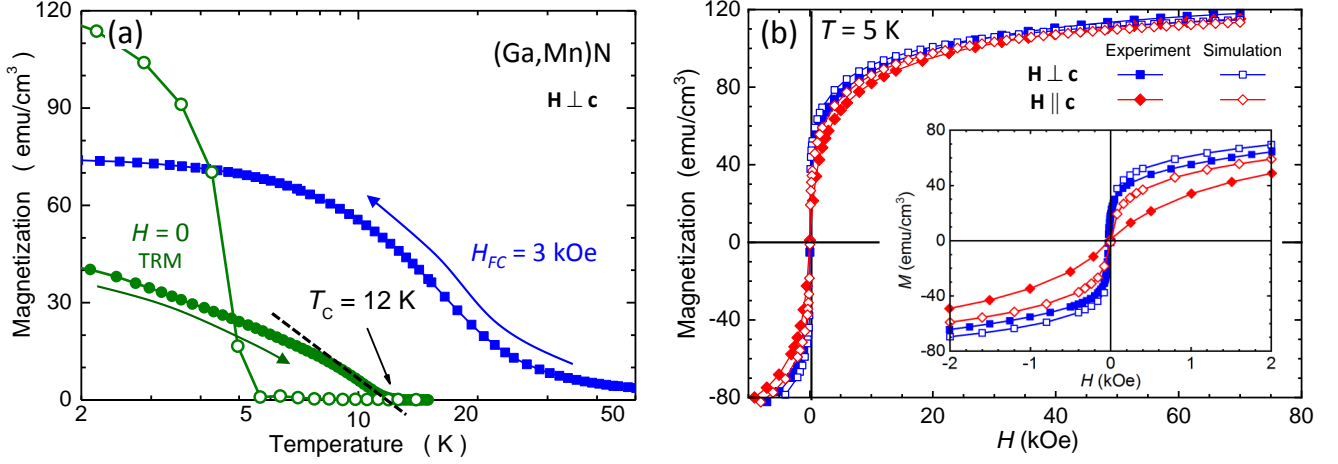


Figure 1. (Color online) Comparison of experimental (solid symbols) and simulated with the atomistic spin model (open symbols) magnetization curves for (Ga,Mn)N film with $x_{\text{Mn}} = 7.9\%$. (a) Temperature dependence of the thermo-remnant magnetization (TRM) for the in-plane orientation of H (full green circles). The initial field-cooled (FC) magnetization measured during cooling at $H_{\text{FC}} = 3$ kOe is shown as solid blue squares. The temperature at which TRM vanishes defines the Curie temperature, T_C , of the film. Open circles represent results from atomistic spin model and Monte Carlo simulations. (b) Magnetization as a function of magnetic field, H , measured at $T = 5$ K for two field orientations: perpendicular to the c -axis (full squares) and along the c -axis (full diamonds), and results of the atomistic spin model added as matched open symbols. The inset provides an expanded view of the low-field region.

$M_{\text{TRM}}(T)$ curve presented in Fig. 1(a) and the $M(H)$ isotherms in Fig. 1(b)—are shown as open symbols. The simulation methodology used to model both dependencies is described in Appendix B. Importantly, these two qualitatively distinct spin-dynamics regimes are simulated using the same set of parameters, which were initially optimized to reproduce the experimental $M(H)$ curves as accurately as possible. As expected, the agreement between the model and experiment is very good for $M(H)$, particularly in the high-field regime. The main quantitative discrepancies appear in the low-field region (as shown in the inset of Fig. 1(b)) and in the simulation of the $M_{\text{TRM}}(T)$ dependence. In both cases, the model tends to overestimate the magnetization at low fields.

These discrepancies originate from three principal limitations of the current modeling approach, which are outlined in more detail in Appendix C. Specifically: (i) the model does not account for pairwise Mn–Mn anisotropy effects [32]; (ii) Jahn–Teller-type anisotropy is approximated using a cubic term; (iii) distribution of Mn ions is assumed to be perfectly random. All these factors contribute to a modified anisotropy landscape, which becomes particularly relevant at low magnetic fields, where the Zeeman energy is insufficient to fully suppress local anisotropy effects. Consequently, the simulated magnetization tends to deviate more strongly from experiment in this regime.

Consequently, achieving a Curie temperature differing

from experiment by only a factor of two can be regarded as a reasonably good result. We mention that doubling the magnitude of exchange integral would indeed reproduce the experimental T_C , but this would produce almost rectangular hysteresis loops with greatly overestimated coercive fields—an outcome clearly at odds with the experiment.

Overall, even though our computational approach captures only a rudimentary level of the real physical complexity in (Ga,Mn)N, the agreement achieved here remains quite notable. It therefore serves as a promising basis for modeling the FMR response of (Ga,Mn)N, as presented in Secs. III C and III D.

B. Temperature dependence of the FMR

Fig. 2 (a) depicts the temperature dependence of the ferromagnetic resonance spectra when \mathbf{H} is applied along the out-of-plane direction ($\mathbf{H} \parallel [0001]$). The hard direction was chosen to minimize the effects of superposition of the FMR signal with the cyclotron resonance (CR) background signal stemming from the conducting GaN template. In contrast to SQUID results, at low temperatures (up to 7 K) only a strong CR and a very weak defect-related paramagnetic signal at $g = 2$ are visible. Ferromagnetic signatures start to appear around $T = 9$ K and their integrated intensity gradually decreases

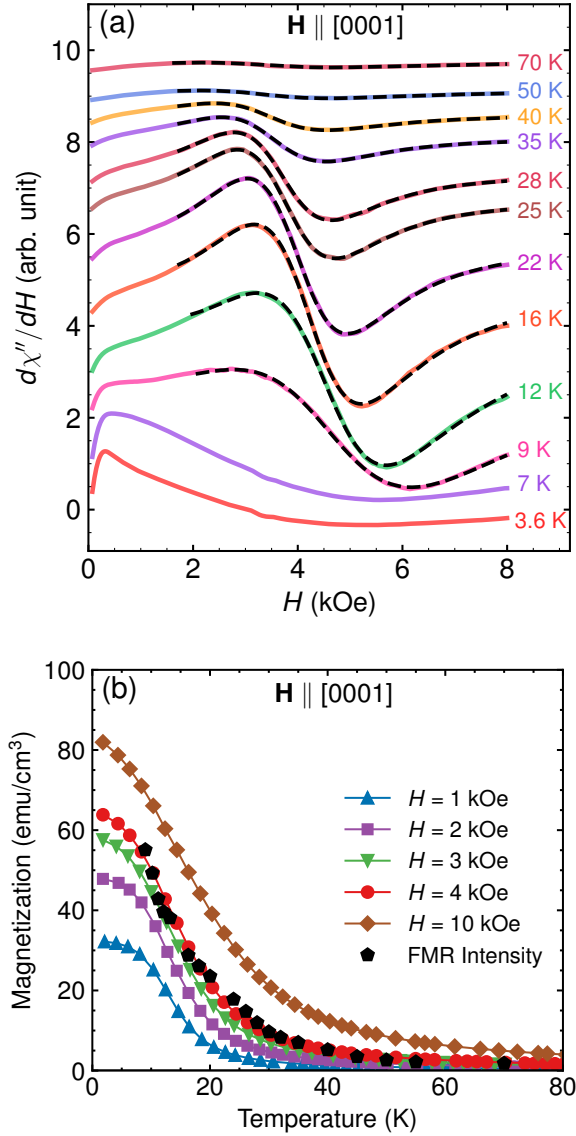


Figure 2. (Color online) (a) Selected, temperature dependent ferromagnetic resonance spectra measured with magnetic field \mathbf{H} applied along the out-of-plane, [0001] crystallographic axis of the (Ga,Mn)N film. The spectra are shifted vertically for clarity. Black dashed lines are fits of Eq. 1. (b) Temperature dependence of the ferromagnetic moment determined by double integration of the FMR signals (pentagons), compared with the magnetization of the (Ga,Mn)N film measured in the same geometry at several magnetic fields H (indicated in the graph).

with increasing temperature to disappear entirely above $T = 70$ K. This behavior is markedly different from that observed in other DFSs, such as (Ga,Mn)As [39, 41, 67], (Ga,Mn)P [42], or the (Pb,Mn)(Te,Se) family [68], where well-defined FMR signals are routinely detected far below the Curie temperature. We attribute the absence of detectable FMR signals below T_C in our (Ga,Mn)N sample

primarily to strong homogeneous broadening, discussed in detail in Section III D. The underlying mechanism remains to be fully elucidated, but it is likely related to an enhanced relaxation rate of the magnetization that causes the resonance to broaden beyond detection limit. A plausible origin of this rapid relaxation lies in the high density of structural defects—particularly threading dislocations—commonly present in (Ga,Mn)N films grown on foreign substrates like sapphire [65, 69].

In order to compare the FMR results with the magnetization measured with SQUID at nonzero magnetic fields we fit the signals with the derivative of a Lorentzian function:

$$\frac{A}{\pi} \frac{d}{dH} \left[\frac{\Delta H}{(H - H_R)^2 + \Delta H^2} + \frac{\Delta H}{(H + H_R)^2 + \Delta H^2} \right], \quad (1)$$

to establish the amplitude A , resonance field H_R , and the half width at half maximum (HWHM) ΔH at each temperature. In the fits we also include the influence of the substrate free electron absorption, which at high enough fields can be approximated by the sum of a decreasing exponential function and a linear increase with H . The fits are denoted by black dashed lines in Fig. 2 (a). The FMR intensity, I , is then calculated as $I = A \times \Delta H$ and is directly proportional to the magnitude of the ferromagnetic moment. In the absence of magnetocrystalline anisotropy it would be possible to obtain absolute values of magnetization from the in- and out-of-plane FMR measurements. This is not the case here. Therefore, we adjust the established intensity of the FMR signal to the magnetization value determined from SQUID at 3 kOe and 55 K. As shown in Fig. 2 (b) a close correspondence is observed between the $M(T)$ values measured between $H = 3$ and 4 kOe and $I(T)$ (pentagons) derived from the FMR data. In both cases the transition temperature exceeds T_C . The fact that the FMR signal persists up to $T = 70$ K is attributed to the magnetic field ($H = 3.3$ kOe) applied in the FMR experiment, which acts against thermal fluctuations [40, 70], and the presence of non-percolating ferromagnetic clusters above T_C .

To substantiate this scenario we re-draw the magnetometry and FMR results in a double logarithmic scale, shown in Fig. 3, since in amorphous systems with a wide range of exchange integrals the magnetic susceptibility, $\chi(T) = M(T)/H$, above their specific coupling temperature is expected to be proportional to $T^{-\alpha}$ [71, 72]. Obviously, $\alpha = 1$ for non-interacting systems (the Curie law) and this dependency is marked by a dashed line in Fig. 3. However, the presence of interactions tends to form spin pairs and higher order complexes which reduce/enhance the magnetization on cooling with respect to T^{-1} for antiferromagnetic/ferromagnetic coupling among the spins.

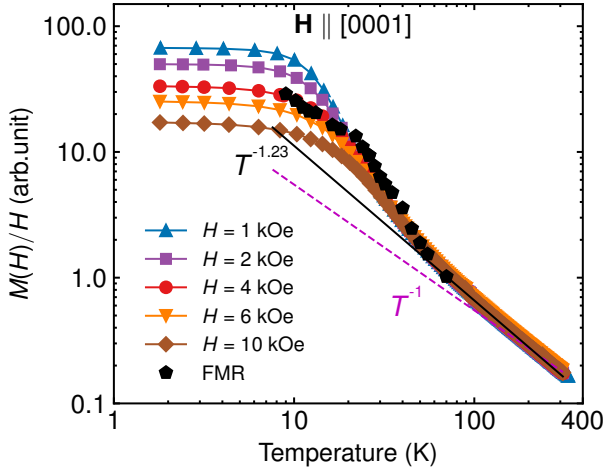


Figure 3. (Color online) Temperature T dependence of the magnetic susceptibility, $\chi(T) = M(T)/H$, measured for the (Ga,Mn)N film in magnetic fields between 1 and 10 kOe, and plotted in a double logarithmic scale (small colored symbols). Black pentagons represent the temperature dependence of the FMR intensity normalized by the resonance field I/H_R . The dashed magenta line indicates the Curie law behavior, i.e. the proportionality to $1/T$, whereas the solid black line follows $\chi(T) \propto T^{-1.23}$ at high temperatures, as expected for a random paramagnet with ferromagnetic correlations.

As a result $\alpha < 1$ for random antiferromagnets. Here Mn- or Co-based II-VI dilute magnetic semiconductors are good examples [73–75]. Analogously, $\alpha > 1$ for ferromagnetic coupling, and (Ga,Mn)N is the prime example here [17]. Our magnetometry data plotted in Fig. 3 follow the same trend as in [17] yielding $\alpha = 1.23$ for $T > 80$ K (marked by the solid black line). This behavior is obeyed at high temperatures independently of the magnitude of H , at least within 1 to 10 kOe range.

However, below $T_f = 70$ K, the entire set of curves deviates upward from the $T^{-1.23}$ trend and begins to fan out below 30 K, without exhibiting any signatures of critical behavior near T_C . The FMR intensity follows a similar trend, with the important observation that the temperature at which the FMR signal rises above the noise level coincides with T_f , i.e. the same temperature at which $\chi(T)$ begins to exceed the values predicted by the quasi-paramagnetic $T^{-1.23}$ dependence. This non-coincidental agreement suggests that T_f marks the onset of formation of sufficiently large ferromagnetically ordered clusters—macrospins—that coherently absorb microwave energy.

One fundamental question arises regarding the nature and size of these FM-coupled entities. Direct quantum-mechanical computations performed on $\text{Ga}_{0.97}\text{Mn}_{0.03}^{3+}\text{N}$, taking into account nearest-neighbor complexes up to the

fourth order (i.e., pairs, triplets, and quartets), showed no deviations from the behavior of noninteracting Mn^{3+} ions in the relevant temperature range [50]. This finding indicates that the FM-like macrospin puddles must contain $N \gg 4$ Mn ions, in accordance with the percolation scenario.

On the other hand, Mn^{3+} ions in GaN have a tendency to cluster [76], and minimizing this effect to achieve a homogeneous Mn distribution required several years of intensive materials research [15, 16, 18, 77]. Despite this substantial technological progress, the resulting layers still exhibit measurable macroscopic inhomogeneities in the spin distribution, yet characterized by a rather small variance $\Delta x \simeq 0.2\%$ [17]. This value appears too low to reflect the presence of relatively small regions with strongly enhanced Mn concentration, as would be expected for spinodal decomposition (chemical phase separation) [78], which is ubiquitously responsible for the room-temperature ferromagnetism in (Ga,Mn)N and related compounds. Resolving this issue requires probes with atomic resolution, such as Atom Probe Tomography, and thus lies beyond the scope of this work.

C. Magnetocrystalline anisotropy

Ferromagnetic resonance is the easiest experimental technique to investigate magnetocrystalline anisotropy. For this purpose we have chosen to rotate the external magnetic field in the $(1\bar{1}00)$ plane, which contains all the relevant crystallographic directions, including the $\langle 100 \rangle$ cubic axes along which static Jahn-Teller distortions occur [79]. However, the low temperature line broadening and the background cyclotron resonance of the GaN template precludes angular dependent investigations below 12 K. The experimental geometry is shown schematically in Fig. 4 (a). Selected FMR spectra recorded for different orientations of the applied magnetic field are presented in Fig. 4 (b), while the angular dependence of the determined resonance fields is given in Fig. 4 (c) (symbols). The solid line in Fig. 4 (c) is calculated with the use of the Smit-Beljers equation [80]:

$$h\nu = \frac{g\mu_B}{M \sin \theta_{eq}} \sqrt{\frac{\partial^2 F}{\partial \theta^2} \frac{\partial^2 F}{\partial \varphi^2} - \left(\frac{\partial^2 F}{\partial \theta \partial \varphi} \right)^2} \bigg|_{\theta_{eq}, \varphi_{eq}}, \quad (2)$$

where $\nu = 9.5$ GHz is the uniform mode resonance frequency, g is the effective spectroscopic splitting factor, μ_B is the Bohr magneton, θ and φ are the polar and azimuthal angles of the magnetization vector, \mathbf{M} , defined in Fig. 4 (a), and F is the anisotropic part of the magnetic free energy density. The equilibrium angles of \mathbf{M} ($\theta_{eq}, \varphi_{eq}$) are determined by minimizing F . In the coor-

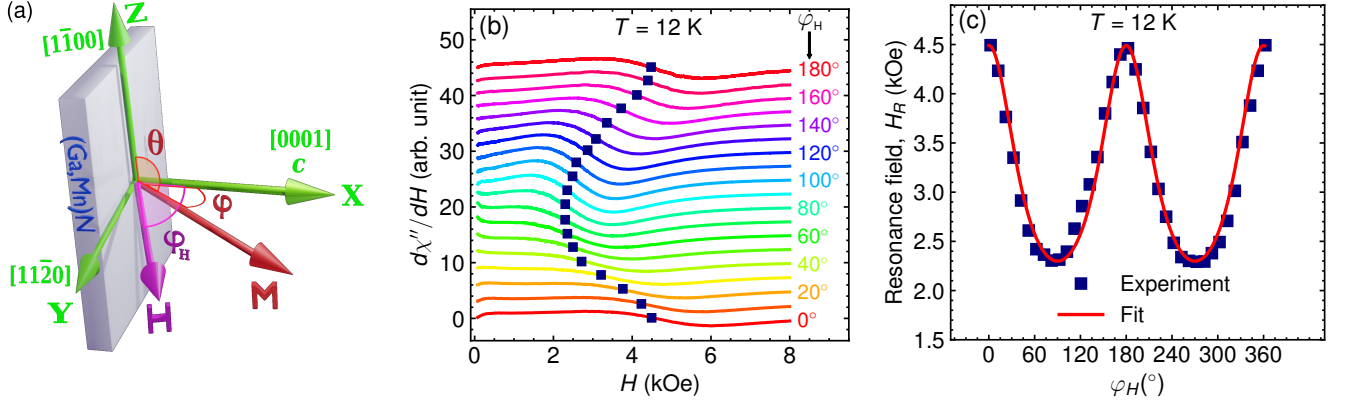


Figure 4. (Color online) (a) Scheme of the FMR measurements geometry emphasizing the coordinate system used. The applied dc magnetic field vector \mathbf{H} lies in the (1100) plane and the azimuthal angle φ_H is counted from the [0001] (X) axis. The orientation of the magnetization vector \mathbf{M} is given by the azimuthal φ and polar θ angles, the latter counted from the [1100] (Z) axis. In principle, \mathbf{H} and \mathbf{M} are not collinear. (b) Selected, angularly dependent ferromagnetic resonance spectra recorded with the magnetic field rotated in the (1100) plane at $T = 12$ K. Symbols indicate resonance field values. (c) Angular dependence of the resonance fields H_R for the magnetic field \mathbf{H} rotated in the (1100) plane at $T = 12$ K. Symbols represent experimental data, the solid line is a fit.

dinate system of Fig. 4 (a) F is given by:

$$F = -MH \sin \theta \cos(\varphi - \varphi_H) + (2\pi M^2 - K_2) \sin^2 \theta \cos^2 \varphi. \quad (3)$$

Here, the first term describes the Zeeman energy, whereas the second term is a combination of the thin film demagnetization energy ($2\pi M^2$) and the uniaxial magnetocrystalline anisotropy energy (K_2) along the [0001] axis. We adhere to the standard convention that the sign of the uniaxial anisotropy is opposite to that defined in the electron paramagnetic resonance Hamiltonian [38]. Higher order terms in F are omitted. Since $\frac{\partial F}{\partial \theta} = 0$ for $\theta_{eq} = 90^\circ$ the magnetization vector also lies in the (1100) rotation plane. Defining an effective uniaxial anisotropy field H_2 as:

$$H_2 = 2\pi M - \frac{K_2}{M} \quad (4)$$

we obtain the following equations:

$$\left(\frac{h\nu}{g\mu_B} \right)^2 = \{H_R \cos(\varphi - \varphi_H) - 2H_2 \cos^2 \varphi\} \times \{H_R \cos(\varphi - \varphi_H) - 2H_2 \cos 2\varphi\}, \quad (5)$$

$$H_R \sin(\varphi - \varphi_H) = H_2 \sin 2\varphi, \quad (6)$$

which can be solved analytically. The relation between φ_H and φ is given by:

$$\varphi_H = \varphi - \arcsin \left(\frac{H_2 \sin 2\varphi}{H_R} \right). \quad (7)$$

The best fit of Eqs.(5)-(7) to the experimental data is shown by solid line in Fig. 4 (c). It yields $H_2 = 0.77$ kOe and $g = 2.29$. The uniaxial anisotropy energy density, determined by subtracting the magnetization value obtained from SQUID measurements at 4 kOe and $T = 12$ K, is $K_2 = -2.1 \times 10^4$ erg/cm³.

The temperature dependence of the uniaxial anisotropy is obtained from FMR signals at two orientations of the applied magnetic field: $\mathbf{H} \parallel [0001]$ ($\varphi_H = 0^\circ$) and $\mathbf{H} \parallel [1120]$ ($\varphi_H = 90^\circ$). The temperature dependencies of H_R for these two field orientations are shown in Fig. 5 (a). With increasing temperature the resonance fields monotonically approach the value corresponding to $g = 2$, characteristic of non-interacting Mn^{3+} ions, as shown by the temperature dependence of the effective g -factor in the inset. This finding is consistent with the magnetic $M(H)/H$ vs. T data (Fig. 3), where deviations from the high-temperature trend $T^{-1.23}$ occur at approximately the same temperature at which g -factor starts to deviate from 2, indicating the onset of detectable ferromagnetic coupling among some Mn^{3+} ions.

The temperature dependence of the effective anisotropy fields H_2 determined from the data presented in Fig. 5 (a) is shown in Fig. 5 (b), together with that of demagnetization fields $2\pi M$ obtained from SQUID measurements at $H = 4$ kOe (Fig. 2 (b)). These two dependencies allow us to approximate the temperature behavior of the uniaxial magnetocrystalline energy density K_2 which is shown in Fig. 5 (d). As can be seen, K_2 is negative in accordance with the fact that the [0001] crystallographic

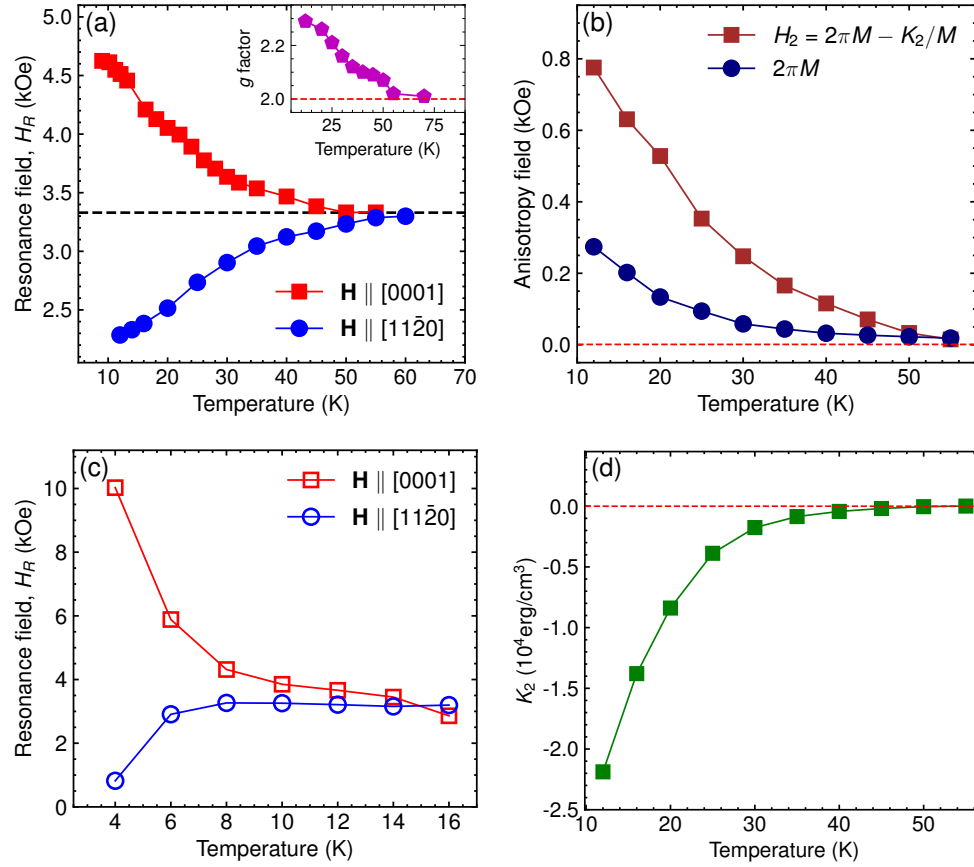


Figure 5. (Color online) (a) Temperature dependence of the resonance fields H_R for two magnetic field orientations: $\mathbf{H} \parallel [0001]$ (squares) and $\mathbf{H} \parallel [11\bar{2}0]$ (circles). The dashed line marks the field corresponding to $g = 2$. The inset shows the temperature dependence of the effective g-factor. (b) Temperature dependence of the anisotropy field H_2 and the demagnetization field $2\pi M$ (squares and circles, respectively). The latter is determined using the magnetization data shown in the inset of Fig. 2 for $H = 4$ kOe. (c) Simulation results depicting the temperature dependence of H_R for two magnetic field orientations: $\mathbf{H} \parallel [0001]$ (open squares) and $\mathbf{H} \parallel [11\bar{2}0]$ (open circles). (d) Temperature dependence of the uniaxial magnetocrystalline anisotropy energy K_2 , obtained from (b). The solid line is a guide for the eye.

axis (c axis) of GaN is the hard magnetization direction in (Ga,Mn)N. With increasing temperature the absolute value of K_2 decreases monotonically to zero.

Figure 5 (c) illustrates the temperature dependence of the resonance field $H_R(T)$ obtained from numerical simulations. As in the experimental data, we analyze two configurations: \mathbf{H} applied along the out-of-plane $[0001]$ direction and the in-plane $[11\bar{2}0]$ direction. The simulation results qualitatively reproduce the experimental trends shown in Fig. 5 (c), albeit in about four times narrower temperature range. However, the same pronounced anisotropy in H_R is observed at low temperatures between the two directions, with the out-of-plane configuration exhibiting significantly larger resonance fields. This anisotropy gradually diminishes with increasing temperature, and H_R converges to approximately the same value as observed in the experiment, about 3.3 kOe.

The low value of the uniaxial anisotropy constant K_2 as compared to those reported for various ferromagnetic transition metals showing room temperature ferromagnetism (e.g. Ref.[38] and references therein) is easily explained bearing in mind the rather moderate magnetic moment resulting both from the low Mn concentration as well as the partial quenching of the spin-orbit interaction (which is the main source of anisotropy in non-metallic ferromagnets) by the Jahn-Teller effect [79]. As the 4-th order terms in the magnetic free energy density are usually an order of magnitude weaker than the uniaxial terms, the lack of such anisotropy terms in the experimental data is not unexpected.

Interestingly, no influence of the static Jahn-Teller distortion on the $H_R(\varphi)$ dependence is observed, contrary to expectations. Specifically, no broadening of the FMR signals is detected along the $\langle 100 \rangle$ cubic axes directions (detailed in the next Section). This result suggests a

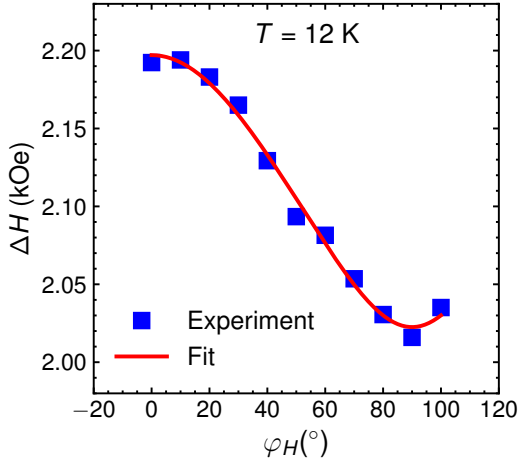


Figure 6. (Color online) Angular dependence of the linewidth ΔH measured at 12 K with the applied magnetic field \mathbf{H} rotated in the $(1\bar{1}00)$ crystal plane (symbols). The line is a fit obtained using the sum of Eqs. (8) and (9) for $\Delta H_{\text{homo}} = 2.07$ kOe and $\Delta H_2 = 63$ Oe.

transition from a static Jahn-Teller effect, previously reported at 2 K [79], to a dynamic regime at $T \simeq 12$ K, where cubic distortion directions are averaged. This observation is intriguing and warrants further investigation.

D. FMR linewidth and relaxation in (Ga,Mn)N

The investigation of the FMR linewidth (ΔH) can give valuable information on the relaxation rate of the magnetization as well as potential inhomogeneities of the studied system. ΔH contains the contributions originating from the intrinsic damping of the magnetization precession, ΔH_{homo} , and the contribution related to magnetic and/or structural inhomogeneities in the system. In the $(1\bar{1}00)$ rotation plane ΔH_{homo} simplifies to [81]:

$$\Delta H_{\text{homo}}(\theta, \varphi) = \left(\frac{\hbar}{g\mu_B} \right)^2 \frac{G\omega}{M \cos(\varphi - \varphi_H)}, \quad (8)$$

where G is the Gilbert damping parameter. One should, therefore, expect minimum linewidths only for two magnetic field directions, since $\varphi_H - \varphi = 0$ only for in-plane and out-of-plane orientations of \mathbf{H} . Instead, the angular dependence of the linewidth measured at 12 K and shown in Fig. 6 resembles that of H_R [Fig. 4 (c)], with maximum and minimum ΔH values at $\mathbf{H} \parallel [0001]$ and $\mathbf{H} \parallel [1\bar{1}\bar{2}0]$, respectively. Such a dependence is expected for inhomogeneous line broadening, arising from a distribution of magnetic moments and anisotropy fields within the sample, which can be expressed as [82]:

$$\Delta H_{\text{inhomo}} = \Delta H_2 \frac{\partial H_R}{\partial H_2}. \quad (9)$$

The fit of experimental data with the sum of Eqs.(8) and (9) presented by the solid line in Fig. 6 gives $\Delta H_{\text{homo}} = 2070$ Oe and $\Delta H_2 = 63$ Oe. In the fit the angular dependence of ΔH_{homo} is neglected since the maximum deviation of ϕ from ϕ_H (at $\phi_H = 50$ deg) leads only to 1.5% line broadening, which falls within the experimental error. It is evident that the main contribution to the linewidth is due to intrinsic damping. The Gilbert parameter determined from Eq. 8 is about $4 \times 10^8 \text{ s}^{-1}$ for \mathbf{H} along $[0001]$ at 12 K and does not differ much from the values found for typical ferromagnetic metals [38]. The reason for the untypically broad linewidth is the low value of magnetization [$M \simeq 45 \text{ emu/cm}^3$, as indicated in Fig. 2 (b)], which enters in the denominator of Eq.(8). This explains also the unusually high value of the parameter $\alpha_G = \frac{\hbar G}{g\mu_B M} = 0.68$ as compared to typical values observed in diluted magnetic systems and metals [38, 83, 84].

The contribution of homogeneous broadening to the total linewidth at 12 K is below 6%, despite the relatively large value of the anisotropy field ($H_2 = 0.77$ kOe). This is attributed to the small relative variation of the anisotropy field, $\Delta H_2/H_2 = 8\%$, which serves as a measure of the spatial inhomogeneity in the Mn distribution. This level of variation is consistent with the previously reported relative standard deviation of Mn concentration, $\Delta x/x \simeq 2 - 4\%$, in similar samples [17].

Fig. 7 (a) illustrates the temperature dependence of ΔH measured for \mathbf{H} applied along the out-of-plane $[0001]$ and in-plane $[1\bar{1}\bar{2}0]$ directions. As shown, the linewidth narrows with increasing temperature in both configurations, reaching minimum values at approximately 26 K and 35 K, as marked in the figure. This narrowing is only partly due to decreasing anisotropy fields [shown in Fig. 5 (b)], but is mostly due to a reduction of the the Gilbert damping parameter G with increasing temperature. The temperature dependence of G extracted from the experimental data is presented in Fig. 7 (c) for in- and out-of-plane magnetic field directions. As can be seen, the damping parameter decreases monotonically with increasing temperature and is consistently greater for the magnetic field applied along the hard axis than for the in plane orientation. The anisotropy of G contributes to the observed difference in the temperature dependencies of the in-plane and out-of-plane linewidths shown in Fig. 7 (a).

The sharp increase in linewidths above the minimum temperatures, up to about 55 K, is attributed to enhanced homogeneous damping associated with the decreasing magnetization of individual clusters, as described by Eq.(8). These clusters contain Mn^{3+} ions

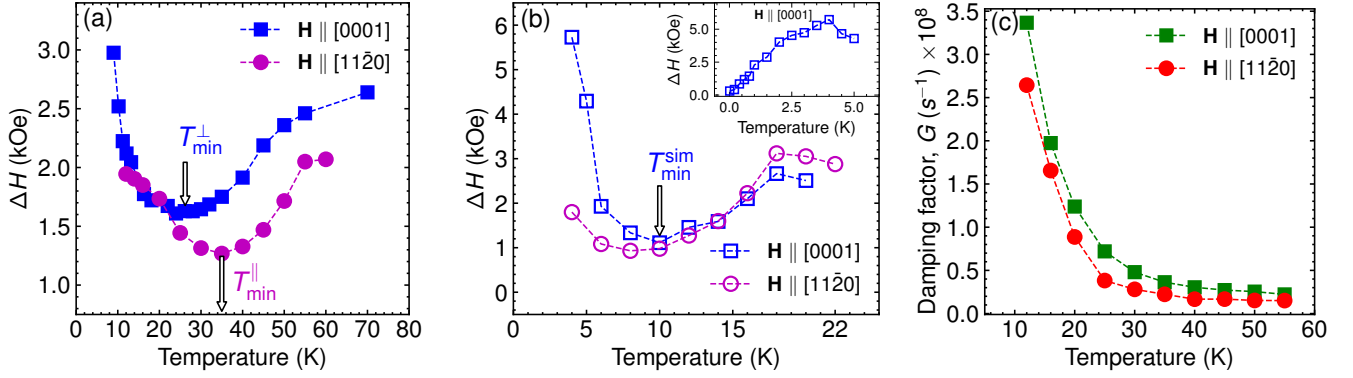


Figure 7. (Color online) (a) Measured temperature dependence of the linewidth ΔH for two magnetic field orientations: $\mathbf{H} \parallel [0001]$ (full squares) and $\mathbf{H} \parallel [11\bar{2}0]$ (full circles). The temperatures at which ΔH attains its minimum values are marked as T_{\min}^{\perp} and T_{\min}^{\parallel} , respectively. (b) Simulated temperature dependence of the linewidth ΔH for the magnetic field orientation $\mathbf{H} \parallel [0001]$ (open squares) and $\mathbf{H} \parallel [11\bar{2}0]$ (open circles). The inset in (b) shows the computed results in a wider temperature range for $\mathbf{H} \parallel [0001]$. (c) Temperature dependence of damping factor, G , for two magnetic field orientations: $\mathbf{H} \parallel [0001]$ (full squares) and $\mathbf{H} \parallel [11\bar{2}0]$ (full circles). Lines are guides for the eye.

that remain sufficiently strongly coupled to produce a detectable FMR signal at temperatures well above 12 K, the Curie temperature of the film determined from direct magnetization measurements.

The observed trend in $\Delta H(T)$ is typical for many ferromagnetic systems [81, 85–87]. The same trend is visible in Fig. 7 (b) which illustrates the temperature dependence of ΔH obtained from simulations. Similar to experimental observations a significant broadening of ΔH is noted at lower temperatures. As the temperature increases, ΔH narrows, reaching a minimum value of 1 kOe at approximately at 10 K denoted by T_{\min}^{sim} . Upon further temperature increase, ΔH slightly broadens again, reaching a maximum at 18 K. Although the obtained values differ from the experimental ones, they are comparable if presented in reduced temperature T/T_C .

IV. SUMMARY

In this study, we have thoroughly investigated the magnetic anisotropy and relaxation dynamics in percolating ferromagnetic semiconductor $\text{Ga}_{1-x}\text{Mn}_x\text{N}$ film with $x \sim 8\%$ using ferromagnetic resonance (FMR) and magnetometry. Our results confirm the ferromagnetic nature of the material, dominated by Mn^{3+} ions, which for this Mn dilution yields a clear ferromagnetic response below $T_C = 12$ K.

While the FMR signal is absent at low temperatures ($T < 9$ K) due to excessive line broadening that prevents detection, the signal persists up to 70 K, revealing the presence of non-percolating FM clusters (macrospins)

above T_C . The temperature dependence of the signal intensity mirrors that of the magnetization up to 55 K, suggesting that the magnetic characteristics of the clusters remain relatively stable across this temperature range. Furthermore, the evolution of the FMR signal with temperature provides direct evidence of the progressive fragmentation of the percolating ferromagnetic network into isolated macrospins.

A crucial observation from our study is that while $(\text{Ga,Mn})\text{N}$ exhibits percolative ferromagnetism, it retains essential features of conventional ferromagnetic materials, particularly in its resonance behavior. The dominance of uniaxial anisotropy with the easy axis perpendicular to the c -axis across the whole temperature range studied here confirms the dominant role of Mn^{3+} single ion magnetic anisotropy. Despite prior reports suggesting the possible influence of static Jahn-Teller distortions, our FMR results do not show evidence of such effects, implying a transition from a static to a dynamic Jahn-Teller regime at the temperatures studied here.

Our atomistic spin model simulations qualitatively reproduce the experimentally observed trends, providing further insights into the nature of ferromagnetic interactions in this dilute system. While the agreement between experiment and simulation is satisfactory, further refinements in modeling Mn-Mn interactions, especially in the presence of short-range disorder, are necessary for more accurate predictions. The combined use of SQUID and FMR techniques allows us to bridge the gap between static and dynamic magnetic properties, illustrating the complex yet highly informative nature of percolating ferromagnetic semiconductors.

In summary, our study confirms that FMR serves as a powerful complementary technique to magnetometry for probing the magnetic behavior of percolating ferromagnetic systems like (Ga,Mn)N. The persistence of FMR signals above T_C highlights the role of non percolating ferromagnetic clusters. Our findings provide new insights into the interplay between magnetization dynamics, anisotropy, and percolation effects in (Ga,Mn)N, contributing to the broader understanding of percolating ferromagnetic systems and their potential relevance for spintronic applications, even well above T_C .

V. ACKNOWLEDGMENTS

The work is supported by the National Science Centre (Poland) through project OPUS 2018/31/B/ST3/03438.

A. MAGNETOMETRY DETAILS

The recorded signals from the (Ga,Mn)N films are weak, below 10^{-6} emu at remanence, and significantly smaller than the signals from the substrate at high magnetic fields [88]. The samples are measured both in perpendicular and in-plane orientations, i. e. with $\mathbf{H} \parallel \mathbf{c}$ or $\mathbf{H} \perp \mathbf{c}$, respectively.

The magnetothermal properties are examined in weak static magnetic fields using standard field-cooled (FC) and thermo-remnant magnetization (TRM) procedures. Special care is taken to ensure an extremely weak residual magnetic field (estimated to be approximately 0.15 Oe) during the TRM measurements. To achieve this condition, the entire system, including the sample, is degaussed at 300 K prior to the TRM measurements by applying an oscillating magnetic field gradually reduced to zero. Subsequently, the sample is field cooled from 300 to 2 K. We underline here that the near-zero field conditions at the base temperature, $T = 2$ K, are established by a soft quench of the MPMS's superconducting magnet. This procedure is carried out using the *magnet reset option* of the MPMS-XL system.

In this respect (Ga,Mn)N and other strongly dilute compounds in which randomly distributed magnetic species are coupled by a short range interaction constitute a class on their own, for which the correct methodology of T_C determination is yet to be firmly established. Earlier studies of criticality in (Ga,Mn)N showed that all the traditional magnetometric approaches, such as the temperature dependence of: AC-susceptibility, the inverse of the static susceptibility, disappearance of the coercive field H_C , as well as of the thermoremanent magnetization

give nearly the same values of the critical temperature [17, 18]. Some small discrepancies among these values are caused by a smeared character of the Curie transition in dilute systems, either due to the formation of magnetic clusters [89] or to the presence of a nonzero variance in the Mn distribution [17].

B. SIMULATION DETAILS

In this Appendix, we provide detailed descriptions of the numerical simulation methodology outlined in the main text, including the complete Hamiltonian, the equations of motion, and the parameter values used in the simulations. The experimental results are modeled in the frame of an atomistic spin model [54] supplemented with stochastic Landau-Lifshitz-Gilbert (sLLG) equation. We use a simulation box of about $25 \times 25 \times 5$ nm³ consisting of approximately 124820 wurtzite lattice cation sites on which the dynamics of 9860 randomly distributed Mn spins ($x = 7.9\%$) is simulated. In-plane periodic boundary conditions are implemented to model a large thin film. We follow the procedure presented in [33].

We use the following Hamiltonian:

$$\mathcal{H} = - \underbrace{\sum_{\langle i,j \rangle} J_{ij} \mathbf{S}_i \cdot \mathbf{S}_j}_{\text{Exchange}} - \underbrace{\frac{1}{4} K^{TR} \sum_i [S_{iz}^2 - (S_{ix}^2 + S_{iy}^2)]}_{\text{Trigonal}} - \underbrace{\frac{1}{2} K^{JT} \sum_i \sum_{j=A,B,C} (\mathbf{S}_i \cdot \mathbf{e}_j^{JT})^4}_{\text{Jahn-Teller}} - \underbrace{\mu_S \sum_i \mathbf{H} \cdot \mathbf{S}_i}_{\text{Zeeman}}, \quad (10)$$

which consists of ferromagnetic superexchange interaction between Mn ions, two terms describing the magnetocrystalline energy, and the Zeeman energy. Here, \mathbf{S}_i describes the normalized local magnetic moment of Mn ion located at site i with magnitude $\mu_S = gS\mu_B$, where $g = 2$, $S = 2$ and μ_B is the Bohr magneton. Mn ions are coupled through a ferromagnetic superexchange interaction of Heisenberg form. We take into account interactions up to the 14th nearest-neighbors approximated by $J_{ij} = J_0 \exp(-R_{ij}/b)$ [19], with R_{ij} being the distance between ions \mathbf{S}_i and \mathbf{S}_j .

The magnetocrystalline energy is composed of (uniaxial) trigonal and Jahn-Teller anisotropies. The latter is approximated by a cubic form [33, 51], with anisotropy axes aligned along the three JT distortion axes, defined after Ref. 31: $e_A^{JT} = [\sqrt{\frac{2}{3}}, 0, \sqrt{\frac{1}{3}}]$, $e_B^{JT} = [-\sqrt{\frac{1}{6}}, -\sqrt{\frac{1}{2}}, \sqrt{\frac{1}{3}}]$, $e_C^{JT} = [-\sqrt{\frac{1}{6}}, \sqrt{\frac{1}{2}}, \sqrt{\frac{1}{3}}]$.

All the numerical results presented in this study are obtained using the following parameter set: $J_{nn} = 4$ meV, $b = 1.1$ Å, $K^{TR} = 0.05$ meV/atom, $K^{JT} = 0.75$ meV/atom, and a Gilbert damping constant $\alpha_G = 0.1$. These values were chosen to achieve the best possible agreement with the experimental magnetization curves $M(H)$ for both anisotropy directions, as shown in Fig. 1 (b).

To calculate the magnetization as a function of external magnetic field $\mathbf{M}(H)$ at a nonzero temperature we initialize the system at a high magnetic field in a completely random spin state. The spin system evolves according to the sLLG equation [33, 51].

$$\frac{\partial \mathbf{S}_i}{\partial t} = -\frac{\gamma}{1 + \alpha_G^2} [\mathbf{S}_i \times \mathbf{H}_{\text{eff}}^{i,tot} + \alpha_G \mathbf{S}_i \times (\mathbf{S}_i \times \mathbf{H}_{\text{eff}}^{i,tot})], \quad (11)$$

where γ and α_G are the gyromagnetic ratio and the precession damping term, respectively. The total effective magnetic field acting on i -th spin $\mathbf{H}_{\text{eff}}^{i,tot}$ consists of the Zeeman, exchange and anisotropy field $\mathbf{H}_{\text{eff}}^i = -(1/\mu_S) \partial \mathcal{H} / \partial \mathbf{S}_i$ and the thermal field \mathbf{H}_{th}^i ([54, 90, 91]. Here \mathbf{H}_{th}^i represents thermal fluctuations (a nonzero temperature) in the system and is modeled as random magnetic field generated in every sLLG iteration according to:

$$\mathbf{H}_{th}^i = \mathbf{\Gamma}(t) \sqrt{\frac{2\alpha_G k_B T}{\gamma \mu_S \Delta t}}, \quad (12)$$

where $\mathbf{\Gamma}(t)$ is a 3D Gaussian random vector with a standard deviation of 1 and mean of zero, and $\Delta t = 5 \cdot 10^{-6}$ ns is the integration time step. The simulation is advanced over time and \mathbf{M} is computed after the system has reached a steady state. This steady-state spin configuration then serves as the initial condition for the subsequent simulation step with a slightly reduced \mathbf{H} . The iterative reduction of \mathbf{H} and corresponding steady-state measurements enable us to construct a detailed $\mathbf{M}(H)$ curve.

To reproduce the TRM data—that is, to calculate the temperature dependence of M at zero magnetic field—we initialize the same numerical box at $T = 0.1$ K, with all Mn spins aligned within the easy plane, i.e., perpendicular to the crystallographic c -axis. This configuration reflects the physical state of the (Ga,Mn)N film after field cooling to the base temperature of the SQUID magnetometer. Subsequently, a very weak probing field of $H = 1$ Oe is applied along the direction of the initial spin alignment, and the system—consisting of nearly 10,000 Mn spins—is allowed to relax toward thermal equilibrium. It is important to note that magnetization-versus-field calculations in the hysteresis region inher-

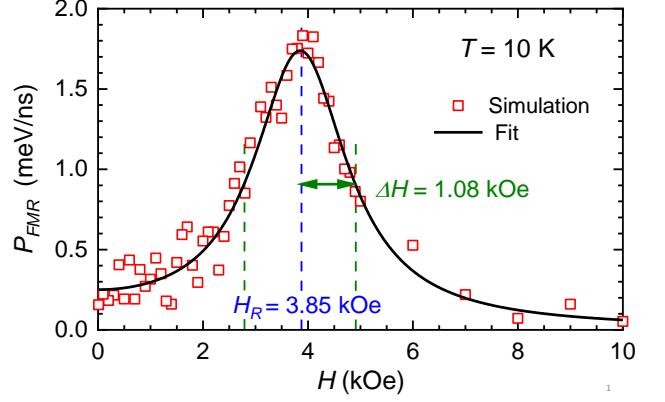


Figure 8. (Color online) Open squares show an example of the simulated ferromagnetic resonance spectrum, obtained within the same framework described here. The solid line represents a fit using a collision-broadened Lorentzian line-shape function (Eq. 13), yielding the resonance field H_R and linewidth ΔH for this particular simulation.

ently correspond to far-from-equilibrium conditions, involving metastable spin configurations. Therefore, the sLLG formalism must be used to capture the dynamics of spin reversal. In contrast, temperature-dependent magnetization data such as $M_{\text{TRM}}(T)$ can be modeled within the framework of thermodynamic equilibrium, which justifies the use of Monte Carlo simulations in this case [54, 92]. Technically, the system is evolved with a sufficient number of Monte Carlo steps per site (MCS/site) [59], where for each MCS, a trial spin orientation change is proposed, and the corresponding energy change ΔE is calculated. The trial move is accepted or rejected based on the Metropolis criterion. The system is considered to have reached equilibrium once the magnetization stabilizes and no significant fluctuations are observed. After determining the resulting M , similarly to the TRM measurement, the simulation proceeds with the temperature increment. Here, the previous spin configuration is used as the initial condition for the next step. The procedure is repeated until the full $M_{\text{TRM}}(T)$ curve is established [60].

To model FMR, we add a sinusoidal AC magnetic field (\mathbf{h}_{AC}) with a frequency $\nu = 9.54$ GHz to the external field \mathbf{H} ensuring that $\mathbf{h}_{AC} \perp \mathbf{H}$ [61]. First, we start with a completely random spin orientation and a very high magnetic field $H = 60$ kOe. The system is allowed to evolve within the sLLG frame until it reaches a steady state, at which we calculate the microwave power absorbed during FMR: $P_{\text{FMR}} = -\frac{\mu_S}{N t_0} \sum_i \int_t^{t+t_0} \mathbf{S}_i \cdot \frac{\partial \mathbf{h}_{AC}(t)}{\partial t} dt$, where N is the number of Mn ions and t_0 is simulation time [61]. Next, this steady-

state spin configuration is used as the initial condition for the next simulation step, in which the external field \mathbf{H} is slightly reduced. This process is repeated iteratively, until \mathbf{H} reaches zero. Exemplary $P_{\text{FMR}}(H)$ simulation data are depicted in Fig. 8 by open symbols.

The resonance field H_R and the line-width ΔH of the simulated FMR are determined at the given T by fitting the collision-broadened Lorentzian line-shape function $f(H)$ [93]:

$$f(H) = \frac{A}{\pi} \left[\frac{\Delta H}{(H - H_R)^2 + \Delta H^2} + \frac{\Delta H}{(H + H_R)^2 + \Delta H^2} \right] \quad (13)$$

to the modeled $P_{\text{FMR}}(H)$. A result of such a fit is represented by solid line in Fig. 8. The entire process is repeated for temperatures ranging from 2 to 22 K.

Technically, in the sLLG simulations, the code is parallelized by dividing the simulation region into sections, with each processor handling a specific part of the system. Computations are accelerated using graphics processing units (GPUs), and Euler's method is employed as the integration scheme after checking that it yields the same results as the Heun's scheme and that all results are stable. Since a higher temperature introduces more disturbance in the system, the initialization and averaging steps of the sLLG simulations are adjusted as specified in table I.

Table I. Parameters of atomistic spin model simulations.

Temperature (K)	Number of initialization steps	Number of averaging steps
0.01 to 0.40	1×10^7	1×10^7
0.60	1×10^7	3×10^7
0.80 to 1.00	1×10^7	4×10^7
1.50	1×10^7	6×10^7
2.00	2×10^7	5×10^7
2.50	2×10^7	6×10^7
3.00 to 3.50	2×10^7	8×10^7
4 to 22	6×10^7	6×10^8

C. LIMITATION OF THE MODEL

While the atomistic spin model employed in this study captures the essential features of the magnetization behavior in (Ga,Mn)N, several simplifying assumptions were made, which limit the accuracy of the simulations—particularly in the low-field regime where the Zeeman

energy is insufficient to overcome subtle anisotropy effects. The primary limitations of the current model are as follows:

- Neglect of Mn–Mn pair anisotropy. Pairwise anisotropic interactions between neighboring Mn ions are not included in the present model. These interactions have been shown to influence magnetic behavior in dilute systems and are currently under intensive investigation in a follow-up study [32]. These effects may be important, as, assuming purely statistical Mn distribution, for $x = 0.08$ as much as $1 - (1 - x)^{12}$ Mn ions, that is 63% of all ions must have at least one nearest-neighbor. Their inclusion is expected to improve the fidelity of the simulated remnant magnetization and coercivity.
- Cubic approximation of Jahn–Teller anisotropy. In reality, the Jahn–Teller effect leads to a tetragonal distortion along one of the cubic $\langle 100 \rangle$ axes, with the trigonal $\langle 111 \rangle$ axis aligned with the crystallographic \mathbf{c} -axis. This implies that the distortion is active along *only* one of the local axes at a time (e_A , e_B , or e_C - defined in the previous section), as captured in direct quantum mechanical calculations and crystal field model [31, 43]. However, such directional specificity (lowering of the site symmetry) cannot be implemented within the classical sLLG framework. Therefore, we approximate the Jahn–Teller contribution using an effective cubic anisotropy term (the second part of Eq. 10), i.e., acting equally along the three crystallographic directions, in contrast to the Jahn–Teller distortion, which selects only one axis at a time.
- Assumption of a perfectly random Mn distribution. The spatial distribution of Mn ions is assumed to be statistically random, without accounting for clustering or local concentration fluctuations that may occur during growth [76]. Experimental and theoretical studies suggest that such inhomogeneities can significantly modify the local anisotropy landscape and spin connectivity, particularly in the dilute regime [17, 18].

Among the above effects, only the pairwise anisotropy is currently being implemented, with preliminary results forming the basis of a separate ongoing study [32]. The inclusion of the remaining contributions—namely, the directional nature of the Jahn–Teller distortion and deviations from random Mn distribution—requires more substantial model development, and is planned for future work.

-
- [1] H. Ohno, Making nonmagnetic semiconductors ferromagnetic, *Science* **281**, 951 (1998).
- [2] T. Dietl, H. Ohno, F. Matsukura, J. Cibert, and D. Fermand, Zener model description of ferromagnetism in zinc-blende magnetic semiconductors, *Science* **287**, 1019 (2000).
- [3] S. Pearton, C. Abernathy, D. Norton, A. Hebard, Y. Park, L. Boatner, and J. Budai, Advances in wide bandgap materials for semiconductor spintronics, *Mater. Sci. Eng. R.* **40**, 137 (2003).
- [4] T. Dietl, H. Ohno, and F. Matsukura, Hole-mediated ferromagnetism in tetrahedrally coordinated semiconductors, *Phys. Rev. B* **63**, 195205 (2001).
- [5] T. Dietl, K. Sato, T. Fukushima, A. Bonanni, M. Jamet, A. Barski, S. Kuroda, M. Tanaka, P. N. Hai, and H. Katayama-Yoshida, Spinodal nanodecomposition in semiconductors doped with transition metals, *Rev. Mod. Phys.* **87**, 1311 (2015).
- [6] M. Iwanska, M. Zajac, B. Lucznik, M. Fijalkowski, M. Amilusik, T. Sochacki, E. Litwin-Staszewska, R. Piotrzkowski, I. Grzegory, and M. Bockowski, Iron and manganese as dopants used in the crystallization of highly resistive HVPE-GaN on native seeds, *Jpn. J. Appl. Phys.* **58**, SC1047 (2019).
- [7] A. Bonanni, M. Sawicki, T. Devillers, W. Stefanowicz, B. Faina, Tian Li, T. E. Winkler, D. Sztenkiel, A. Navarro-Quezada, M. Rovezzi, R. Jakiela, A. Grois, M. Wegscheider, W. Jantsch, J. Suffczyński, F. D'Acapito, A. Meingast, G. Kothleitner, and T. Dietl, Experimental probing of exchange interactions between localized spins in the dilute magnetic insulator (Ga,Mn)N, *Phys. Rev. B* **84**, 035206 (2011).
- [8] T. Yamamoto, H. Sazawa, N. Nishikawa, M. Kiuchi, T. Ide, M. Shimizu, T. Inoue, and M. Hata, Reduction in buffer leakage current with Mn-doped GaN buffer layer grown by metal organic chemical vapor deposition, *Jpn. J. Appl. Phys.* **52**, 08JN12 (2013).
- [9] L. Janicki, G. Kunert, M. Sawicki, E. Piskorska-Hommel, K. Gas, R. Jakiela, D. Hommel, and R. Kudrawiec, Fermi level and bands offsets determination in insulating (Ga,Mn)N/GaN structures, *Sci. Rep.* **7**, 41877 (2017).
- [10] J. Kreissl, W. Ulrici, M. El-Metoui, A. -M. Vasson, A. Vasson, and A. Gavaix, Neutral manganese acceptor in GaP: An electron-paramagnetic-resonance study, *Phys. Rev. B* **54**, 10508 (1996).
- [11] T. Dietl, Origin and control of ferromagnetism in dilute magnetic semiconductors and oxides (invited), *J. Appl. Phys.* **103**, 07D111 (2008).
- [12] J. Blinowski, P. Kacman, and J. A. Majewski, Ferromagnetic superexchange in Cr-based diluted magnetic semiconductors, *Phys. Rev. B* **53**, 9524 (1996).
- [13] M. Sawicki, T. Devillers, S. Gałęski, C. Simserides, S. Dobkowska, B. Faina, A. Grois, A. Navarro-Quezada, K. N. Trohidou, J. A. Majewski, T. Dietl, and A. Bonanni, Origin of low-temperature magnetic ordering in $\text{Ga}_{1-x}\text{Mn}_x\text{N}$, *Phys. Rev. B* **85**, 205204 (2012).
- [14] C. Śliwa and T. Dietl, Tight-binding theory of spin-spin interactions, Curie temperatures, and quantum hall effects in topological (Hg,Cr)Te in comparison to nontopological (Zn,Cr)Te and (Ga,Mn)N, *Phys. Rev. B* **110**, 165201 (2024).
- [15] E. Sarigiannidou, F. Wilhelm, E. Monroy, R. M. Galera, E. Bellet-Amalric, A. Rogalev, J. Goulon, J. Cibert, and H. Mariette, Intrinsic ferromagnetism in wurtzite (Ga,Mn)N semiconductor, *Phys. Rev. B* **74**, 041306(R) (2006).
- [16] G. Kunert, S. Dobkowska, Tian Li, H. Reuther, C. Kruse, S. Figge, R. Jakiela, A. Bonanni, J. Grenzer, W. Stefanowicz, J. von Borany, M. Sawicki, T. Dietl, and D. Hommel, $\text{Ga}_{1-x}\text{Mn}_x\text{N}$ epitaxial films with high magnetization, *Appl. Phys. Lett.* **101**, 022413 (2012).
- [17] S. Stefanowicz, G. Kunert, C. Simserides, J. A. Majewski, W. Stefanowicz, C. Kruse, S. Figge, Tian Li, R. Jakiela, K. N. Trohidou, A. Bonanni, D. Hommel, M. Sawicki, and T. Dietl, Phase diagram and critical behavior of a random ferromagnet $\text{Ga}_{1-x}\text{Mn}_x\text{N}$, *Phys. Rev. B* **88**, 081201(R) (2013).
- [18] K. Gas, J. Z. Domagala, R. Jakiela, G. Kunert, P. Dłuzewski, E. Piskorska-Hommel, W. Paszkowicz, D. Sztenkiel, M. J. Winiarski, D. Kowalska, R. Szukiewicz, T. Baraniecki, A. Miszczuk, D. Hommel, and M. Sawicki, Impact of substrate temperature on magnetic properties of plasma-assisted molecular beam epitaxy grown (Ga,Mn)N, *J. Alloys Compd* **747**, 946 (2018).
- [19] A. Bonanni, T. Dietl, and H. Ohno, Dilute magnetic materials, in *Handbook on Magnetism and Magnetic Materials*, edited by J. M. D. Coey and S. S. P. Parkin (Springer, Berlin, 2021).
- [20] M. Sawicki, Magnetic properties of (Ga,Mn)As, *J. Magn. Magn. Mater* **300**, 1 (2006).
- [21] T. Jungwirth, J. Mašek, K. Y. Wang, K. W. Edmonds, M. Sawicki, M. Polini, J. Sinova, A. H. MacDonald, R. P. Campion, L. X. Zhao, N. R. S. Farley, T. K. Johal, G. van der Laan, C. T. Foxon, and B. L. Gallagher, Low-temperature magnetization of (Ga,Mn)As semiconductors, *Phys. Rev. B* **73**, 165205 (2005).
- [22] T. Jungwirth, K. Y. Wang, J. Mašek, K. W. Edmonds, J. König, J. Sinova, M. Polini, N. A. Goncharuk, A. H. MacDonald, M. Sawicki, R. P. Campion, L. X. Zhao, C. T. Foxon, and B. L. Gallagher, Prospects for high temperature ferromagnetism in (Ga,Mn)As semiconductors, *Phys. Rev. B* **72**, 165204 (2005).
- [23] J. Sadowski, S. Kret, A. Šiušys, T. Wojciechowski, K. Gas, M. F. Islam, C. M. Canali, and M. Sawicki, Wurtzite (Ga,Mn)As nanowire shells with ferromagnetic properties, *Nanoscale* **9**, 2129 (2017).
- [24] L. Gluba, O. Yastrubchak, J. Z. Domagala, R. Jakiela, T. Andrearczyk, J. Żuk, T. Wosinski, J. Sadowski, and M. Sawicki, Band structure evolution and the origin of

- magnetism in (Ga,Mn)As: From paramagnetic through superparamagnetic to ferromagnetic phase, *Phys. Rev. B* **97**, 115201 (2018).
- [25] M. Sawicki, D. Chiba, A. Korbecka, Y. Nishitani, J. A. Majewski, F. Matsukura, T. Dietl, and H. Ohno, Experimental probing of the interplay between ferromagnetism and localization in (Ga,Mn)As, *Nat. Phys.* **6**, 22 (2010).
- [26] O. Proselkov, D. Sztienkiel, W. Stefanowicz, M. Aleszkiewicz, J. Sadowski, T. Dietl, and M. Sawicki, Thickness dependent magnetic properties of (Ga,Mn)As ultrathin films, *Appl. Phys. Lett.* **100**, 262405 (2012).
- [27] L. Chen, F. Matsukura, and H. Ohno, Electric-field modulation of damping constant in a ferromagnetic semiconductor (Ga,Mn)As, *Phys. Rev. Lett.* **115**, 057204 (2015).
- [28] T. Dietl, Interplay between carrier localization and magnetism in diluted magnetic and ferromagnetic semiconductors, *J. Phys. Soc. Jpn.* **77**, 031005 (2008).
- [29] M. A. Mayer, P. R. Stone, N. Miller, H. M. Smith, O. D. Dubon, E. E. Haller, K. M. Yu, W. Walukiewicz, X. Liu, and J. K. Furdyna, Electronic structure of $\text{Ga}_{1-x}\text{Mn}_x\text{As}$ analyzed according to hole-concentration-dependent measurements, *Phys. Rev. B* **81**, 045205 (2010).
- [30] A. Richardella, P. Roushan, S. Mack, B. Zhou, D. A. Huse, D. D. Awschalom, and A. Yazdani, Visualizing critical correlations near the metal-insulator transition in $\text{Ga}_{1-x}\text{Mn}_x\text{As}$, *Science* **327**, 665 (2010).
- [31] J. Gosk, M. Zajac, A. Wolos, M. Kaminska, A. Twardowski, I. Grzegory, M. Bockowski, and S. Porowski, Magnetic anisotropy of bulk GaN:Mn single crystals codoped with Mg acceptors, *Phys. Rev. B* **71**, 094432 (2005).
- [32] K. Das, N. G. Szewacki, R. Hayn, and D. Sztienkiel, Jahn-Teller effect and pair anisotropy in wurtzite $\text{Ga}_{1-x}\text{Mn}_x\text{N}$ [10.48550/ARXIV.2410.22035](https://arxiv.org/abs/2410.22035) (2024).
- [33] D. Sztienkiel, K. Gas, N. G. Szewacki, M. Foltyn, C. Śliwa, T. Wojciechowski, J. Domagala, D. Hommel, M. Sawicki, and T. Dietl, Electric field manipulation of magnetization in an insulating dilute ferromagnet through piezoelectromagnetic coupling, *Commun. Mater.* **6**, 16 (2025).
- [34] W. Stefanowicz, D. Sztienkiel, B. Faina, A. Grois, M. Rovezzi, T. Devillers, F. d'Acapito, A. Navarro-Quezada, Tian Li, R. Jakiela, M. Sawicki, T. Dietl, and A. Bonanni, Structural and paramagnetic properties of dilute $\text{Ga}_{1-x}\text{Mn}_x\text{N}$, *Phys. Rev. B* **81**, 235210 (2010).
- [35] D. Sztienkiel, M. Foltyn, G. P. Mazur, R. Adhikari, K. Kosiel, K. Gas, M. Zgierski, R. Kruszka, R. Jakiela, Tian Li, A. Piotrowska, A. Bonanni, M. Sawicki, and T. Dietl, Stretching magnetism with an electric field in a nitride semiconductor, *Nat. Commun.* **7**, 13232 (2016).
- [36] H. Nakayama, M. Althammer, Y.-T. Chen, K. Uchida, Y. Kajiwara, D. Kikuchi, T. Ohtani, S. Geprägs, M. Opel, S. Takahashi, R. Gross, G. E. W. Bauer, S. T. B. Goennenwein, and E. Saitoh, Spin Hall magnetoresistance induced by a nonequilibrium proximity effect, *Phys. Rev. Lett.* **110**, 206601 (2013).
- [37] J. A. Mendoza-Rodarte, K. Gas, M. Herrera-Zaldívar, D. Hommel, M. Sawicki, and M. H. D. Guimarães, Spin Hall magnetoresistance in Pt/(Ga,Mn)N devices, *Appl. Phys. Lett.* **125**, 152404 (2024).
- [38] M. Farle, Ferromagnetic resonance of ultrathin metallic layers, *Rep. Prog. Phys.* **61**, 755 (1998).
- [39] X. Liu, Y. Sasaki, and J. K. Furdyna, Ferromagnetic resonance in $\text{Ga}_{1-x}\text{Mn}_x\text{As}$: Effects of magnetic anisotropy, *Phys. Rev. B* **67**, 205204 (2003).
- [40] Y. Sasaki, X. Liu, J. K. Furdyna, M. Palczewska, J. Szczytko, and A. Twardowski, Ferromagnetic resonance in GaMnAs, *J. Appl. Phys.* **91**, 7484 (2002).
- [41] Y. Y. Zhou, X. Liu, J. K. Furdyna, M. A. Scarpulla, and O. D. Dubon, Ferromagnetic resonance investigation of magnetic anisotropy in $\text{Ga}_{1-x}\text{Mn}_x\text{As}$ synthesized by ion implantation and pulsed laser melting, *Phys. Rev. B* **80**, 224403 (2009).
- [42] C. Bihler, M. Kraus, H. Huebl, M. S. Brandt, S. T. B. Goennenwein, M. Opel, M. A. Scarpulla, P. R. Stone, R. Farshchi, and O. D. Dubon, Magnetocrystalline anisotropy and magnetization reversal in $\text{Ga}_{1-x}\text{Mn}_x\text{P}$ synthesized by ion implantation and pulsed-laser melting, *Phys. Rev. B* **75**, 214419 (2007).
- [43] A. Wolos, M. Palczewska, M. Zajac, J. Gosk, M. Kaminska, A. Twardowski, M. Bockowski, I. Grzegory, and S. Porowski, Optical and magnetic properties of Mn in bulk GaN, *Phys. Rev. B* **69**, 115210 (2004).
- [44] A. Wolos, A. Wyszomolek, M. Kaminska, A. Twardowski, M. Bockowski, I. Grzegory, S. Porowski, and M. Potemski, Neutral Mn acceptor in bulk GaN in high magnetic fields, *Phys. Rev. B* **70**, 245202 (2004).
- [45] K. G. et al., Magnetic anisotropy of paramagnetic Mn^{3+} in GaN (2025), manuscript in preparation.
- [46] J. T. Vallin, G. A. Slack, S. Roberts, and A. E. Hughes, Infrared absorption in some II-VI compounds doped with Cr, *Phys. Rev. B* **2**, 4313 (1970).
- [47] J. T. Vallin and G. D. Watkins, EPR of Cr^{2+} in II-VI lattices, *Phys. Rev. B* **9**, 2051 (1974).
- [48] M. Herbich, W. Mac, A. Twardowski, K. Ando, Y. Shapira, and M. Demianiuk, Magnetization and exciton spectroscopy of the diluted magnetic semiconductor $\text{Cd}_{1-x}\text{Cr}_x\text{S}$, *Phys. Rev. B* **58**, 1912 (1998).
- [49] T. Graf, M. Gjukic, M. S. Brandt, M. Stutzmann, and O. Ambacher, The $\text{Mn}^{3+/2+}$ acceptor level in group III nitrides, *Appl. Phys. Lett.* **81**, 5159 (2002).
- [50] D. Sztienkiel, K. Gas, J. Domagala, D. Hommel, and M. Sawicki, Crystal field model simulations of magnetic response of pairs, triplets and quartets of Mn^{3+} ions in GaN, *New. J. Phys.* **22**, 123016 (2020).
- [51] Y. K. Edathumkandy and D. Sztienkiel, Comparative study of magnetic properties of Mn^{3+} magnetic clusters in GaN using classical and quantum mechanical approach, *J. Magn. Magn. Mater.* **562**, 169738 (2022).
- [52] Simserides, C., Majewski, J.A., Trohidou, K.N., and Dietl, T., Theory of ferromagnetism driven by superexchange in dilute magnetic semiconductors, *EPJ Web of Conferences* **75**, 01003 (2014).
- [53] K. Sato, L. Bergqvist, J. Kudrnovský, P. H. Dederichs, O. Eriksson, I. Turek, B. Sanyal, G. Bouzerar, H. Katayama-Yoshida, V. A. Dinh, T. Fukushima,

- H. Kizaki, and R. Zeller, First-principles theory of dilute magnetic semiconductors, *Rev. Mod. Phys.* **82**, 1633 (2010).
- [54] R. F. L. Evans, W. J. Fan, P. Chureemart, T. A. Ostler, M. O. A. Ellis, and R. W. Chantrell, Atomistic spin model simulations of magnetic nanomaterials, *J. Phys.: Condens. Matt.* **26**, 103202 (2014).
- [55] M. Sawicki, W. Stefanowicz, and A. Ney, Sensitive SQUID magnetometry for studying nanomagnetism, *Semicon. Sci. Technol.* **26**, 064006 (2011).
- [56] L. M. C. Pereira, J. P. Araújo, M. J. V. Bael, K. Temst, and A. Vantomme, Practical limits for detection of ferromagnetism using highly sensitive magnetometry techniques, *J. Phys. D: Appl. Phys.* **44**, 215001 (2011).
- [57] K. Gas and M. Sawicki, In situ compensation method for high-precision and high-sensitivity integral magnetometry, *Meas. Sci. Technol.* **30**, 085003 (2019).
- [58] K. Gas and M. Sawicki, A simplified method of the assessment of magnetic anisotropy of commonly used sapphire substrates in SQUID magnetometers, *Materials* **15**, 10.3390/ma15238532 (2022).
- [59] Y. Zhang, B. Wang, Y. Guo, Q. Li, and J. Wang, A universal framework for metropolis Monte Carlo simulation of magnetic Curie temperature, *Comput. Mater. Sci.* **197**, 110638 (2021).
- [60] V. V. Prudnikov, P. V. Prudnikov, and D. E. Romanovskiy, Monte Carlo simulation of magnetic multilayered structures with giant magnetoresistance effects, *J. Phys. Conf. Ser.* **681**, 012016 (2016).
- [61] K. D. Usadel, Temperature-dependent dynamical behavior of nanoparticles as probed by ferromagnetic resonance using Landau-Lifshitz-Gilbert dynamics in a classical spin model, *Phys. Rev. B* **73**, 212405 (2006).
- [62] K. Fabian, V. P. Shcherbakov, and S. A. McEnroe, Measuring the curie temperature, *Geochemistry, Geophysics, Geosystems* **14**, 947 (2013).
- [63] M. Wang, K. W. Edmonds, B. L. Gallagher, A. W. Rushforth, O. Makarovskiy, A. Patané, R. P. Campion, C. T. Foxon, V. Novak, and T. Jungwirth, High Curie temperatures at low compensation in the ferromagnetic semiconductor (Ga,Mn)As, *Phys. Rev. B* **87**, 121301 (2013).
- [64] K. Gas, A. Królicka, K. Dybko, P. Nowicki, Z. Khosravizadeh, T. Story, and M. Sawicki, Magnetic constitution of topologically trivial thermoelectric PbTe:Cr, *J. Magn. Magn. Mater.* **537**, 168154 (2021).
- [65] K. Kalbarczyk, K. Dybko, K. Gas, D. Sztienkiel, M. Foltyn, M. Majewicz, P. Nowicki, E. Łusakowska, D. Hommel, and M. Sawicki, Electrical characteristics of vertical-geometry Schottky junction to magnetic insulator (Ga,Mn)N heteroepitaxially grown on sapphire, *Journal of Alloys and Compounds* **804**, 415 (2019).
- [66] D. Sztienkiel, Spin orbital reorientation transitions induced by magnetic field, *Journal of Magnetism and Magnetic Materials* **572**, 170644 (2023).
- [67] X. Liu and J. K. Furdyna, Ferromagnetic resonance in $\text{Ga}_{1-x}\text{Mn}_x\text{As}$ dilute magnetic semiconductors, *J. Phys. Condens. Matter* **18**, R245 (2006).
- [68] T. Story, P. J. T. Eggenkamp, C. H. W. Swüste, H. J. M. Swagten, W. J. M. de Jonge, and A. Szczerbakow, Magnetic-resonance study of the diluted magnetic semiconductor $\text{pb}_{1-x-y}\text{sn}_y\text{mn}_x\text{te}$, *Phys. Rev. B* **47**, 227 (1993).
- [69] J. W. P. Hsu, M. J. Manfra, D. V. Lang, S. Richter, S. N. G. Chu, A. M. Sargent, R. N. Kleiman, L. N. Pfeiffer, and R. J. Molnar, Inhomogeneous spatial distribution of reverse bias leakage in gan schottky diodes, *Applied Physics Letters* **78**, 1685 (2001), <https://doi.org/10.1063/1.1356450>.
- [70] P. R. Stone, M. A. Scarpulla, R. Farshchi, I. D. Sharp, E. E. Haller, O. D. Dubon, K. M. Yu, J. W. Beeman, E. Arenholz, J. D. Denlinger, and H. Ohldag, Mn $L_{3,2}$ x-ray absorption and magnetic circular dichroism in ferromagnetic $\text{Ga}_{1-x}\text{Mn}_x\text{P}$, *Appl. Phys. Lett.* **89**, 012504 (2006).
- [71] R. N. Bhatt, Magnetic properties of doped semiconductors, *Phys. Scr.*, **T14**, 7 (1986).
- [72] J. R. Anderson, M. Górka, L. J. Azevedo, and E. L. Venturini, Magnetization of $\text{Hg}_{1-x}\text{Mn}_x\text{Te}$, *Phys. Rev. B* **33**, 4706 (1986).
- [73] R. N. Bhatt and P. A. Lee, Scaling studies of highly disordered spin-1/2 antiferromagnetic systems, *Phys. Rev. Lett.* **48**, 344 (1982).
- [74] T. Dietl, Localization and magnetic interactions in semimagnetic semiconductors at low temperatures, *Jpn. J. Appl. Phys.* **26**, 1907 (1987).
- [75] M. Sawicki, E. Guzewicz, M. I. Łukasiewicz, O. Proselkov, I. A. Kowalik, W. Lisowski, P. Dłuzewski, A. Wittlin, M. Jaworski, A. Wolska, W. Paszkowicz, R. Jakiela, B. S. Witkowski, L. Wachnicki, M. T. Klepka, F. J. Luque, D. Arvanitis, J. W. Sobczak, M. Krawczyk, A. Jablonski, W. Stefanowicz, D. Sztienkiel, M. Godlewski, and T. Dietl, Homogeneous and heterogeneous magnetism in (Zn,Co)O: From a random antiferromagnet to a dipolar superferromagnet by changing the growth temperature, *Phys. Rev. B* **88**, 085204 (2013).
- [76] N. Gonzalez Szwacki, J. A. Majewski, and T. Dietl, Aggregation and magnetism of Cr,Mn, and Fe cations in GaN, *Phys. Rev. B* **83**, 184417 (2011).
- [77] W. Stefanowicz, D. Sztienkiel, B. Faina, A. Grois, M. Rovezzi, T. Devillers, A. Navarro-Quezada, Tian Li, R. Jakiela, M. Sawicki, T. Dietl, and A. Bonanni, Structural and paramagnetic properties of dilute $\text{Ga}_{1-x}\text{Mn}_x\text{N}$, *Phys. Rev. B* **81**, 235210 (2010).
- [78] A. Bonanni and T. Dietl, A story of high-temperature ferromagnetism in semiconductors, *Chem. Soc. Rev.* **39**, 528 (2010).
- [79] A. Wolos, A. Wyszomolek, M. Kaminska, A. Twardowski, M. Bockowski, I. Grzegory, S. Porowski, and M. Potemski, Neutral Mn acceptor in bulk GaN in high magnetic fields, *Phys. Rev. B* **70**, 245202 (2004).
- [80] J. Smit and H. G. Beljers, *Philips Res. Rep.* **10**, 113 (1955).
- [81] W. Platow, A. N. Anisimov, G. L. Dunifer, M. Farle, and K. Baberschke, Correlations between ferromagnetic-

- resonance linewidths and sample quality in the study of metallic ultrathin films, *Phys. Rev. B* **58**, 5611 (1998).
- [82] C. Chappert, K. L. Dang, P. Beauvillain, H. Hurdequint, and D. Renard, Ferromagnetic resonance studies of very thin cobalt films on a gold substrate, *Phys. Rev. B* **34**, 3192 (1986).
- [83] J. Sinova, T. Jungwirth, X. Liu, Y. Sasaki, J. K. Furdyna, W. A. Atkinson, and A. H. MacDonald, Magnetization relaxation in (Ga,Mn)As ferromagnetic semiconductors, *Phys. Rev. B* **69**, 085209 (2004).
- [84] Y. Matsuda, A. Oiwa, K. Tanaka, and H. Muneoka, Ferromagnetic resonance study of magnetization relaxation in GaMnAs, *Physica B* **376-377**, 668 (2006), proceedings of the 23rd International Conference on Defects in Semiconductors.
- [85] Y. Li, M. Farle, and K. Baberschke, Critical spin fluctuations and curie temperatures of ultrathin Ni(111)/W(110): A magnetic-resonance study in ultrahigh vacuum, *Phys. Rev. B* **41**, 9596 (1990).
- [86] J. Kötztler and H. von Philipsborn, Critical speeding-up of spin-relaxation in CdCr₂Se₄, *Phys. Rev. Lett.* **40**, 790 (1978).
- [87] F. Spörel and E. Biller, Electron spin resonance in nickel near T_c , *Solid State Commun.* **17**, 833 (1975).
- [88] K. Gas, G. Kunert, P. Dłuzewski, R. Jakiela, D. Hommel, and M. Sawicki, Improved-sensitivity integral SQUID magnetometry of (Ga,Mn)N thin films in proximity to Mg-doped GaN, *J. Alloys Compd* **868**, 159119 (2021).
- [89] R. B. Griffiths, Nonanalytic behavior above the critical point in a random Ising ferromagnet, *Phys. Rev. Lett.* **23**, 17 (1969).
- [90] B. Skubic, J. Hellsvik, L. Nordström, and O. Eriksson, A method for atomistic spin dynamics simulations: implementation and examples, *J. Phys.: Condens. Matt.* **20**, 315203 (2008).
- [91] R. F. L. Evans, U. Atxitia, and R. W. Chantrell, Quantitative simulation of temperature-dependent magnetization dynamics and equilibrium properties of elemental ferromagnets, *Phys. Rev. B* **91**, 144425 (2015).
- [92] D. Szentkiel, Introducing the step monte carlo method for simulating dynamic properties, *Advanced Theory and Simulations* **6**, 2300184 (2023).
- [93] J. H. Van Vleck and V. F. Weisskopf, On the shape of collision-broadened lines, *Rev. Mod. Phys.* **17**, 227 (1945).